NASA/TM-95- 207298

# Navier–Stokes Computations on Full Wing–Body Configuration with Oscillating Control Surfaces

Shigeru Obayashi, Ing-Tsau Chiu,
Guru P. Guruswamy

Reprinted from

**Journal of Aircraft**

Volume 32, Number 6, Pages 1227–1233

AIAA

*A publication of the*
American Institute of Aeronautics and Astronautics, Inc.
370 L'Enfant Promenade, SW
Washington, DC 20024-2518

JOURNAL OF AIRCRAFT
Vol. 32, No. 6, November–December 1995

IN-02-TM
076 01

# Navier–Stokes Computations on Full Wing–Body Configuration with Oscillating Control Surfaces

Shigeru Obayashi,* Ing-Tsau Chiu,† and Guru P. Guruswamy‡
*NASA Ames Research Center, Moffett Field, California 94035*

**Unsteady Navier–Stokes simulations have been performed for vortical flows over an "arrow-wing" configuration of a supersonic transport in the transonic regime. Computed steady pressures and integrated force coefficients with and without control surface deflection at a moderate angle of attack are compared with experiment. For unsteady cases, oscillating trailing-edge control surfaces are modeled by using moving grids. Response characteristics between symmetric and antisymmetric oscillatory motions of the control surfaces on the left and right wings are studied. The antisymmetric case produces higher lift than the steady case with no deflection and the unsteady symmetric case produces higher lift than the antisymmetric case. The detailed analysis of the wake structure revealed a strong interaction between the primary vortex and the wake vortex sheet from the flap region when the flap is deflected up.**

## Introduction

ACCURATE prediction of aeroelastic loads is necessary for the design of large flexible aircraft. Uncertainties in the characteristics of loads may result in an improper accounting for aeroelastic effects, leading to understrength or overweight designs and unacceptable fatigue life. Moreover, correct prediction of loads and the resultant structural deformations is essential to the determination of the aircraft stability and control characteristics. Since the experimental evaluation would involve considerable cost and the risk of structural damage in a wind tunnel it is necessary to initiate the investigation through theoretical analyses.

Critical design conditions occur in the transonic regime by mixed flow, embedded shocks, separation, and vortical flow. Furthermore, aircraft are often subject to aeroelastic oscillation because of the flow unsteadiness. In this unsteady aerodynamic environment, many modern aircraft rely heavily on active controls for safe and steady flight operation.

An arrow-wing configuration has been studied as a design concept for supersonic civil transport.[1] Because of the highly swept thin wing, it is known that transonic flutter is a design problem on this configuration.[2] Development of an analytical tool to predict aerodynamic and aeroelastic performance of arrow-wing configurations is essential to advance supersonic transport technology.

The present investigation is initiated in conjunction with a recently developed code, ENSAERO, which is capable of computing aeroelastic responses by simultaneously integrating the Euler/Navier–Stokes equations and the modal structural equations of motion using aeroelastically adaptive dynamic grids.[3–6] The code has been applied to transonic flows from small to moderately large angles of attack for fighter wings undergoing unsteady motions. The code was extended to simulate unsteady flows over a rigid wing with an oscillating trailing-edge flap. In this research, the geometric capability of the code has further been extended to handle a full-span wing–body configuration with control surfaces.

This article reports the results of unsteady Navier–Stokes simulations of transonic flows over a rigid arrow-wing body configuration with oscillating control surfaces. Computations have been made with and without control surface deflections. Computed pressures and integrated force coefficients have been compared with the wind-tunnel experiment.[1] Comparison of response characteristics between symmetric and antisymmetric control surface motions on the right and left wings is also presented.

## Numerical Method

The nondimensionalized Reynolds-averaged thin-layer Navier–Stokes equations are used in this study. The viscosity coefficient is computed as the sum of the laminar and turbulent viscosity coefficients where the laminar viscosity is taken from the freestream laminar viscosity, assumed to be constant for transonic flows. As an option, Sutherland's law can be used to calculate the laminar viscosity. The turbulent viscosity is evaluated by the Baldwin–Lomax algebraic eddy-viscosity model.[7] Since the flowfield considered in this article contains leading-edge separation, a modification to the turbulence model originally developed for crossflow-type separation[8] is applied.

Several numerical schemes have been developed to solve the Navier–Stokes equations. The present code has two different schemes for the inviscid term: 1) the central-difference and 2) streamwise upwind schemes. A second-order central-difference evaluation is applied to the viscous term. An implicit method is used for the time integration because it is more suitable for expensive unsteady viscous calculations. A complete description of the algorithm can be found in Ref. 4. Specific code performance information for the current study is given as follows. All results were computed on Cray computers at NASA Ames Research Center and the Numerical Aerodynamic Simulation (NAS) Program. The performance of the upwind version of ENSAERO for the moving grid case is 400 MFLOPS and 8.6 $\mu$s per iteration per grid point on a single Cray-C90 processor (175 MFLOPS and 18.4 $\mu$s on a single Cray Y-MP processor).

## Model Geometry and Grid

The H-H topology grid is used for a wing–body configuration with a control surface. This topology is chosen in order

Received June 14, 1993; presented as Paper 93-3687 at the AIAA Atmospheric Flight Mechanics Conference, Monterey, CA, Aug. 9–11, 1993; revision received May 15, 1995; accepted for publication May 15, 1995. Copyright © 1995 by the American Institute of Aeronautics and Astronautics, Inc. No copyright is asserted in the United States under Title 17, U.S. Code. The U.S. Government has a royalty-free license to exercise all rights under the copyright claimed herein for Governmental purposes. All other rights are reserved by the copyright owner.

*Senior Research Scientist; currently Associate Professor, Tohoku University, Sendai, Japan. Senior Member AIAA.
†Research Scientist; currently at Overset Methods Inc., 262 Marich Way, Los Altos, CA 94022. Member AIAA.
‡Research Scientist. Associate Fellow AIAA.

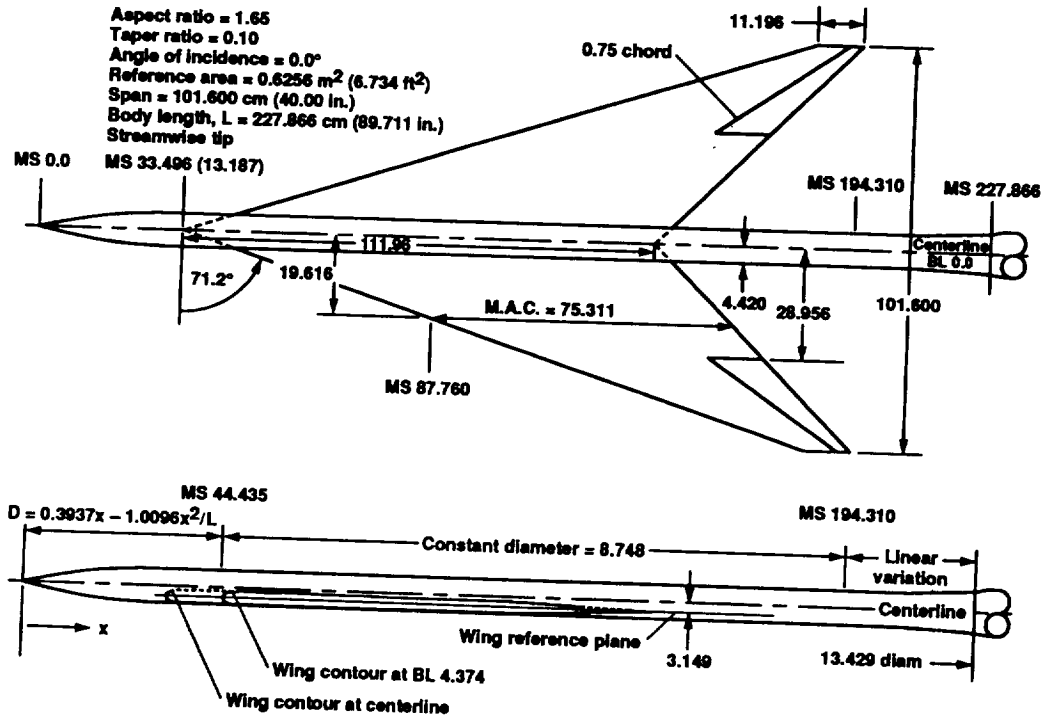


Fig. 1 Wind-tunnel model geometry of an arrow-wing configuration (all dimensions in centimeters).

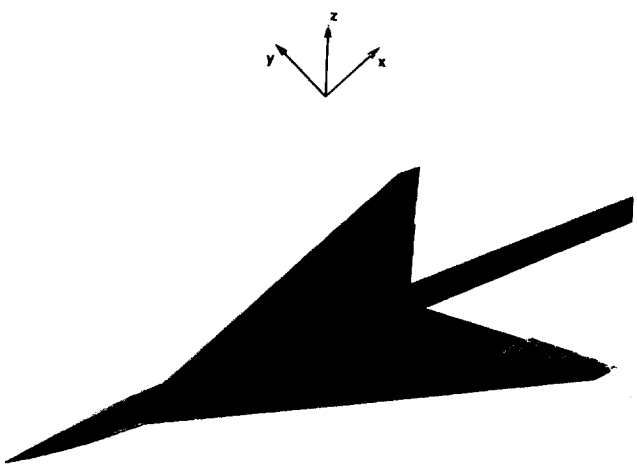


Fig. 2 Overview of the surface grid.

to easily align grid lines to the control surface. The ICEM DDN CAD software system[9] was used to generate the surface grid. From the surface grid, the volume grid was generated by using HYPGEN code.[10] Although the experimental model[1] has two flaps both at the leading and trailing edges, only the outboard flap at the trailing edge is considered in this article. Figure 1 shows the geometry of the wind-tunnel model. The configuration has a thin, low aspect ratio, highly swept wing mounted below the centerline of a slender body. The wing is flat with a rounded leading edge. It should be noted that the exact wingtip definition was not available and so the tip thickness was decreased to zero across three grid points.

Figure 2 shows the overview of the surface grid for the full-span configuration (the grid lines on the wing are shown for every other line). The reference length is taken from the mean aerodynamic chord and the origin of the coordinates is set at the nose of the body. The body is extended to the downstream boundary. The half-span grid used for the symmetric cases consists of 110 points in the streamwise direction, 116 points in the spanwise direction, and 40 points normal to the body surface, for a total of 510,400 points. The bilateral symmetry condition is imposed in the $x$-$z$ plane at $y = 0$ (the center of the body). In the following computations, the grid is further divided into the upper and lower grids at the wing and the H-topology cut condition is provided through a zonal interface. For the full-span configuration used for the antisymmetric cases, the grid is mirrored to the other side (total of four zones), and thus, the number of grid points is doubled to 1,020,800 points. Flow variables at the zonal interfaces were updated as soon as the adjoining zones were computed. This gives a semi-implicit zonal interface for steady-state calculations. The same procedure can be applied to unsteady calculations by alternating the sweep through zones at every time step.

To treat the control surface movement without introducing additional zones, a small gap is introduced at the end of the control surface. This region is used to shear the grid when the control surface oscillates. The dynamic grid around a deflected control surface was obtained by shearing every grid line normal to the control surface with the local deflection, $\Delta x$ and $\Delta z$.

In the experiment, a transition strip was placed at the 15% chord. However, the report did not show significant differences in comparisons of force measurement with and without the strip at the transonic regime.[1] In addition, the effect of the strip on the separation at the leading edge was not very clear. Thus, in the computation, a fully turbulent flow is assumed.

The grid lines on the body surface collapse to a point at the nose and extend upstream as a singular axis. The flow variables on the singular axis are given by taking an average from the surrounding grid points. When a computation starts impulsively from the freestream condition, the upwind method is not dissipative enough to damp the initial disturbances along the axis. The central-difference option of the code was used to overcome this initial transient period. Since the upwind solution gave a crisper vortex structure for steady state, the upwind option was used for the rest of the calculations.

## Results

### Steady Flap Deflection

Figure 3 shows the steady pressures compared with the experiment at the 20, 50, and 80% semispanwise sections for the half-span configuration. The 80% section is located in the mid span of the control surface. The flow conditions consist of a Mach number of $M_\infty = 0.85$, an angle of attack of $\alpha = 7.93$ deg, a flap deflection of $\delta = 0$ deg, and a Reynolds number of $Re_c = 9.5 \times 10^6$ based on the mean aerodynamic chord. Suction observed near the trailing edge at the 80% section corresponds to the leading-edge vortex. There is a minor discrepancy between the computation and the experiment due to the difference in the location of the leading-edge vortex. The computation predicts the vortex at a slightly more inboard location than the experiment. Possible sources of this difference are the effects of the transition strip and the wall of the wind tunnel. No data correction was applied to either the computed or measured data. Overall, the computed result shows good agreement with the experiment. The pressure distributions on the body center also show good agreement as shown in Fig. 4.

The corresponding result at the same flow condition with the flap deflected down by 8.3 deg is shown in Fig. 5. The effect of the flap deflection is apparent at the 80% spanwise section, although no streamwise separation is found on the flap surface. The kinks in the pressure profiles at the 75% chord correspond to the flap hinge. At the 50% spanwise section, the effect of the flap deflection is only found near the trailing edge. The effect is not noticeable at the 20% section. The computed pressure profiles capture the flow features well. The effect of the flap deflection is very small on the body, and thus, the pressure distributions are not shown here.

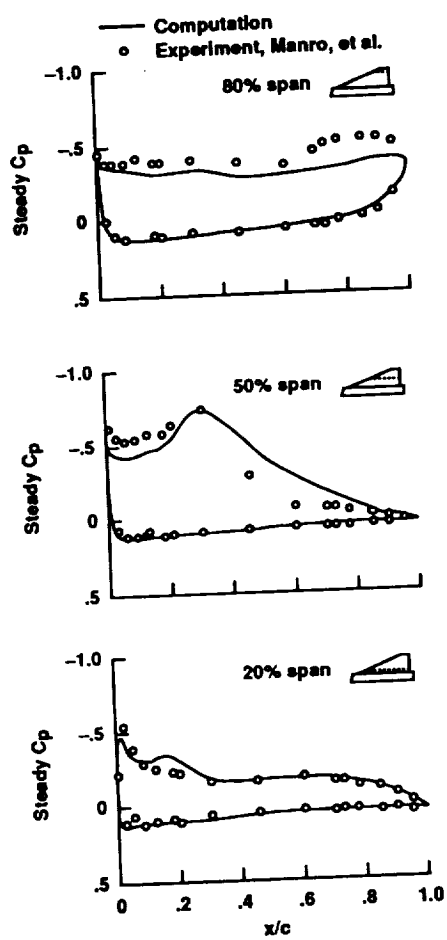


Fig. 3 Comparison of computed steady pressures with experiment; no flap deflection.

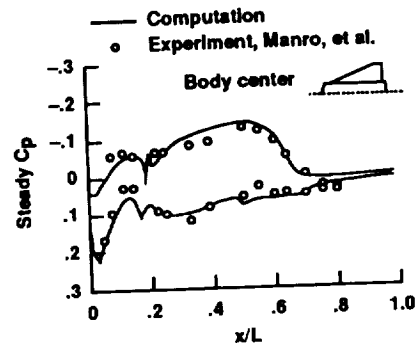


Fig. 4 Comparison of computed steady pressures with experiment on the body surface; no flap deflection.

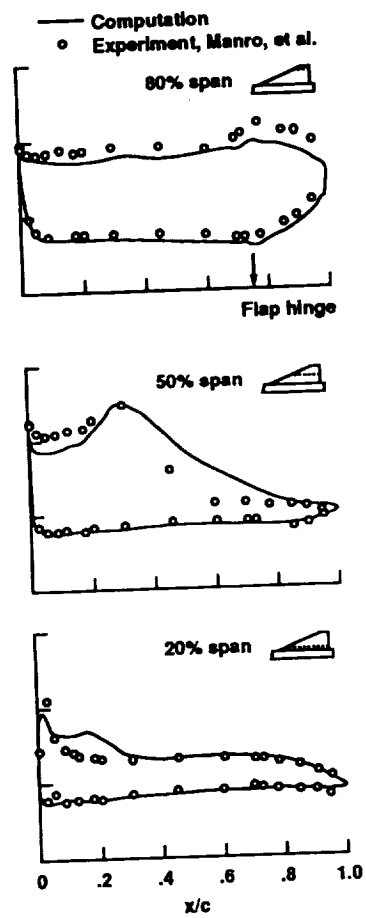


Fig. 5 Comparison of computed steady pressures with experiment; 8.3-deg flap deflection.

Table 1 shows the comparison of force coefficients. Both normal force and moment coefficients show good agreement with the experimental data. The lift coefficients are 0.346 and 0.310 with and without flap deflection, respectively.

Figure 6 shows the steady pressures for the full-span configuration with antisymmetric flap position. The right wing has the flap up by 8.3 deg and the left wing has the flap down by 8.3 deg. The pressure distributions show the largest difference between the left and right wings at the 80% section, as expected. The plot also shows a discrepancy between the antisymmetric case and the symmetric case with the flap deflected down. The antisymmetric position of the flaps generates a lower pressure above the left wing and a higher pressure above the right wing. This introduces a circulation around

Table 1 Comparison of force coefficients with experiment

| | $\alpha$ = 7.93 deg, $\delta$ = 0 deg | | $\alpha$ = 7.93 deg, $\delta$ = 8.30 deg | |
|---|---|---|---|---|
| | $C_N$ | $C_{M_y}$ | $C_N$ | $C_{M_y}$ |
| Computation | 0.298 | −0.063 | 0.332 | −0.092 |
| Experiment[1] | 0.295 | −0.065 | 0.328 | −0.093 |

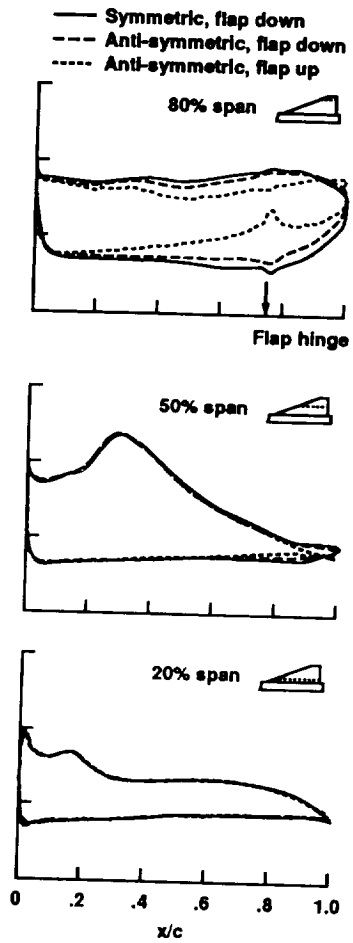


Fig. 6 Comparison of computed steady pressures between the symmetric and antisymmetric flap deflections.

the $x$ axis. Therefore, at the 80% section, the antisymmetric result shows smaller $\Delta C_p$ (and thus, smaller sectional lift) than the symmetric result.

Figure 7 illustrates the structure of the vortical flowfield for the antisymmetric case by using the helicity density. Figure 7a corresponds to the trailing edge. Note that the helicity density was computed on the grid points, and thus, the crossflow view here is not exactly the $y$-$z$ plane at a constant $x$ location. The other plots are taken downstream at intervals of approximately 0.03 and 0.06$\bar{c}$. The primary and secondary vortices can be found over both wings. The wingtip vortices can barely be found next to the secondary vortices. An interesting feature is that the wake vortex sheet shed from the flap region rolls up and merges with the secondary vortex. As the flap is deflected up, the rolled-up vortex sheet becomes closer to the primary vortex. Due to the interaction by the primary vortex, the rolled-up vortex is displaced towards the secondary vortex, and thus, they merge more quickly. On the other hand, the vortex interaction is moderate when the flap is down. Instead, the vortex itself is stronger because of the camber introduced by the deflected flap. Without the flap deflection, the corresponding wake structure basically falls into the middle of the left and right wake structures.

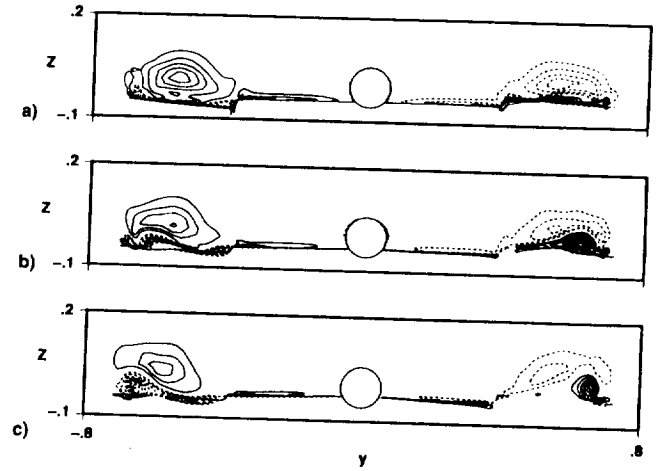


Fig. 7 Crossflow helicity density contour plots in the wake for the antisymmetric case: a) trailing edge, b) 0.03$\bar{c}$ downstream, and c) 0.06$\bar{c}$ downstream.

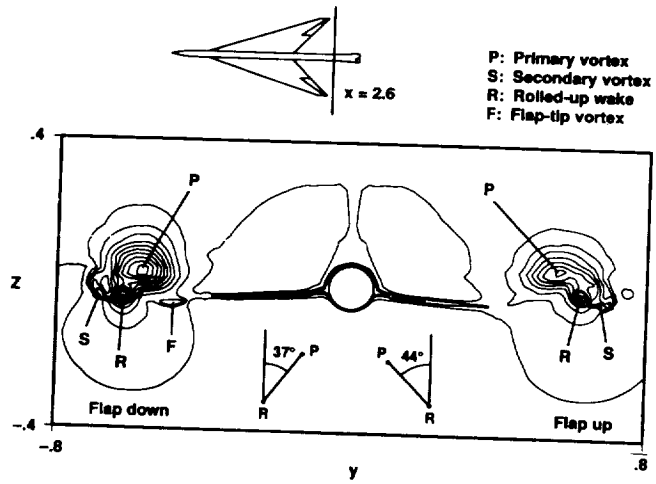


Fig. 8 Crossflow density contour plots at $x$ = 2.6 for the antisymmetric case.

The density contour plot in the crossflow plane (the true $y$-$z$ plane) at $x$ = 2.6 is shown in Fig. 8. The right half of the plot corresponds to the wake for the upward flap position and the left half corresponds to the wake for the downward flap position. On the left-hand side (LHS), four low-density regions can be found: 1) the primary vortex $P$, 2) secondary vortex $S$, 3) rolled-up wake vortex sheet $R$, and 4) the flap inboard-tip vortex $F$. The wingtip vortex is weaker than these vortices and is not clearly observed here. The secondary vortex and the rolled-up wake vortex sheet are really the same vortical region and they merge rapidly as shown in Fig. 7. The flap inboard-tip vortex can be seen only on the left side where the flap is deflected down. On the right-hand side (RHS), three low-density regions are found. Comparing the height of the two primary vortices, the left one is located lower due to the flap deflected down. Also, the lower density at the center of the left primary vortex indicates a stronger vorticity. When we draw a line connecting the center of the primary vortex and the center of the rolled-up wake vortex sheet, the line makes a 37-deg angle to the vertical on the LHS, while the corresponding line makes a 44-deg angle on the RHS. Thus, the rolled-up vortex sheet on the RHS is displaced more toward the secondary vortex.

### Oscillatory Flap Motion

The capability of ENSAERO code used in this work to compute unsteady flows with oscillating flaps is previously

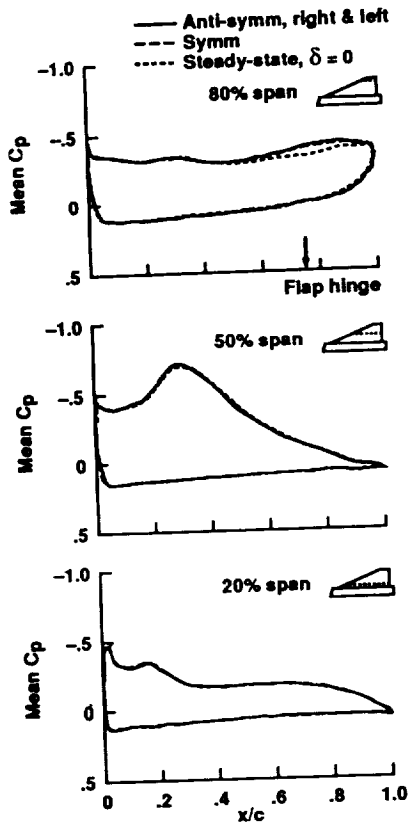


Fig. 9 Comparison of computed mean pressures between the symmetric and antisymmetric oscillatory motions of the flaps.

validated with the measured data for a wing and detailed results are reported in Ref. 6. In this section, similar unsteady computations are made for the wing–body configuration shown in Fig. 1. It is noted that measured unsteady data is not available for this wing–body configuration.

The flow conditions for the oscillatory cases were chosen to be the same as the steady cases: $M_\infty = 0.85$, $\alpha = 7.93$ deg, and $Re_c = 9.5 \times 10^6$. The flap oscillates at a reduced frequency of $k = 0.6$ (approximately 15 Hz) and an amplitude of $\delta = 8.3$ deg. There is no mean deflection of the flap. The symmetric motion assumes the same flap motion both on the left and right wings, and thus, uses the half-span grid. The antisymmetric motion results in a 180-deg phase difference in the flap motions on the left and right wings and uses the full-span grid.

The nondimensional time step size used was about 0.0025 (5000 steps per cycle, this number was determined by accuracy considerations based on the experience in Ref. 6). Two cycles of the flap motion were computed from the steady-state solution with no flap deflection. To verify the time accuracy, the time step size was set to about 0.0016 (7500 steps per cycle) at the third cycle. Since the second and third cycle gave the same pressure responses, the solution converged to a periodic solution with sufficient time accuracy.

Figure 9 shows the comparison of the time-averaged pressures obtained from both symmetric and antisymmetric flap oscillations with the steady-state solution for the undeflected flap case. For the antisymmetric case, the right and left wings produce identical pressure profiles because the difference of the flap motion is only in the phase angle. The symmetric case shows almost identical profiles to the antisymmetric case. Both the unsteady results show larger $\Delta C_p$ at the 80% section than the steady result. This indicates that the unsteady cases

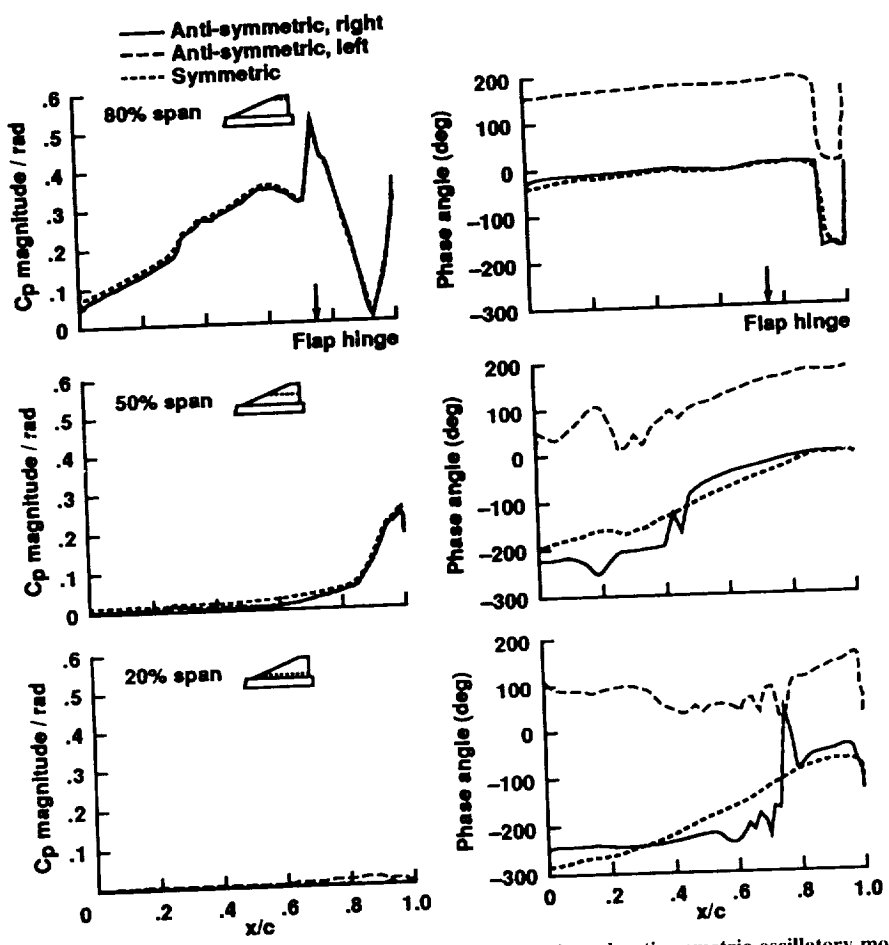


Fig. 10 Comparison of computed unsteady pressures between the symmetric and antisymmetric oscillatory motions of the flaps.

have slightly higher lift on the average (the lift responses are shown later).

Unsteady pressure responses to the flap motion are shown in magnitude and phase angle in Fig. 10. In the magnitude plots, the left and right wings for the antisymmetric case give identical responses again because the only difference in the flap motion is the 180-deg phase angle. Also, antisymmetric results show slightly lower responses than the symmetric result because the 180-deg phase difference cancels the pressure variation at the body centerline. At the 80% spanwise section, a sharp peak is found at the hinge line of the control surface, which is located at the 75% chord. After the 90% chord, the magnitude of $C_p$ drops and rises again near the trailing edge. A similar trend can be found at the 50% spanwise section. In the phase plots, the left and right wings for the antisymmetric case clearly show a 180-deg phase difference at the 80% section. Corresponding to the magnitude plot at this section, a jump of the phase change by 180 deg can be found around the 90% chord. This unsteady response is related to the interaction between the primary vortex and the wake vortex sheet as explained later.

At the inboard sections, the phase plots for the antisymmetric case are not as smooth as those for the symmetric case. The 180-deg phase difference between the left and right wings is not seen, either. Since the magnitude for the antisymmetric case is nearly zero in this region, the phase plots for the antisymmetric case are more sensitive to numerical errors. Second-order time accuracy may be needed to achieve a perfect 180-deg phase difference for reasonable time step sizes. The result was not improved very much by simply halving the time step size. For practical purposes, the current result is accurate enough because the instantaneous $C_p$ plots on the left wing still coincide with those of the right wing after a half cycle (180-deg difference).

Figure 11 shows the instantaneous density contour plots in the crossflow plane (true $y$-$z$ plane) at $x = 2.6$, similar to Fig. 8. Five instances were chosen at 0-, 45-, 90-, 135-, and 180-deg phase angles. The left wing starts from 0 deflection, goes down, and comes back to 0 deflection. The right flap starts from 0 deflection, goes up, and comes back to 0 deflection. The rest of the half cycle is a mirror image of this half cycle. By comparing Figs. 11a and 11c, the left primary vortex goes down and becomes stronger as the flap goes down and the right primary vortex goes up and becomes weaker as the flap goes up.

When we draw lines connecting the center of the primary vortex and the center of the rolled-up wake vortex sheet, the angles that the line on the RHS make with the vertical line vary more than the corresponding angles on the LHS. This indicates that the primary vortex has a stronger influence on the wake vortex sheet from the flap when it goes up. This explains the pressure response near the trailing edge at the 80% section observed earlier in Fig. 10. It also explains the 180-deg phase jump because the disturbance occurs when the flap is up, which is negative deflection-by-definition.

By comparing Figs. 11b and 11d, a slight discrepancy can be found in the vortex structure. This suggests hysteresis in the lift response. Figure 12 shows the lift responses with respect to the flap deflection angle of the right wing. As observed in Fig. 11, the right wing shows the hysteresis as the flap is deflected up (negative deflection). The total lift response shows that the unsteady case has more lift than the steady case ($C_L = 0.310$).

The symmetric case shows the hysteresis when the flap is deflected down. This increase in the lift is associated with the primary vortex enhanced by the downward deflection of the flap. The overall lift for the symmetric case is higher than the antisymmetric case. This is consistent to the steady pressure result shown in Fig. 6. On the other hand, the antisymmetric case introduces a circulation around the $x$ axis as discussed earlier in the steady results. This circulation reduces the strength

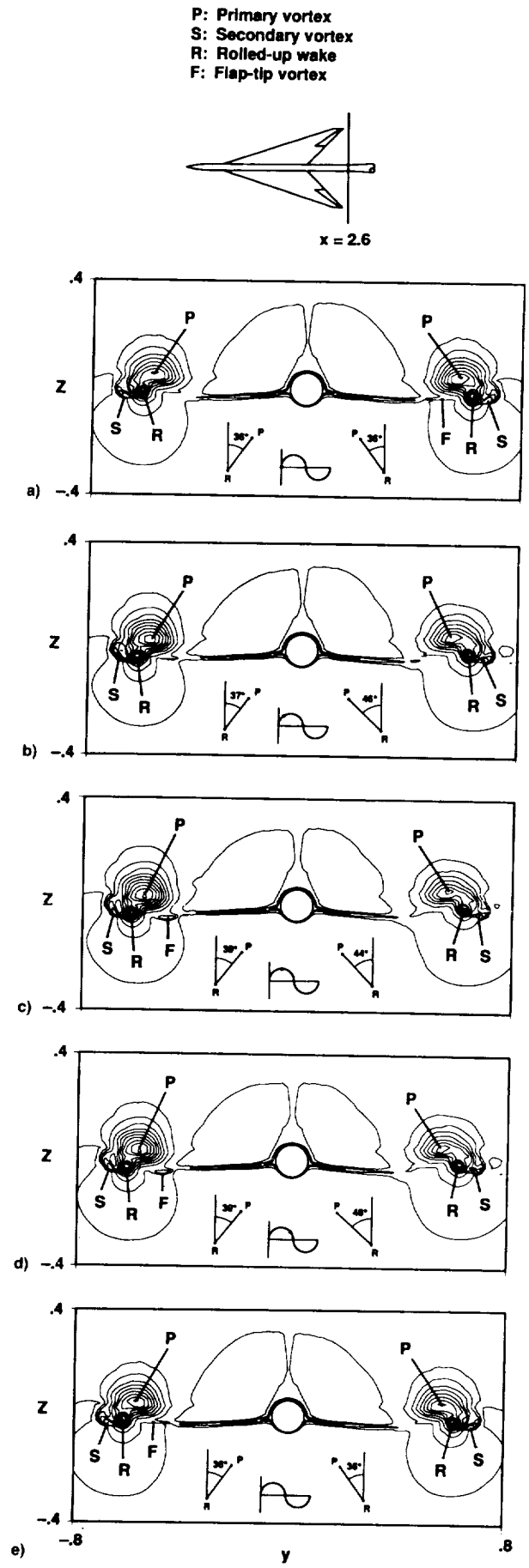


**Fig. 11 Crossflow density contour plots at $x = 2.6$ for the antisymmetric oscillatory motion of the flaps.**

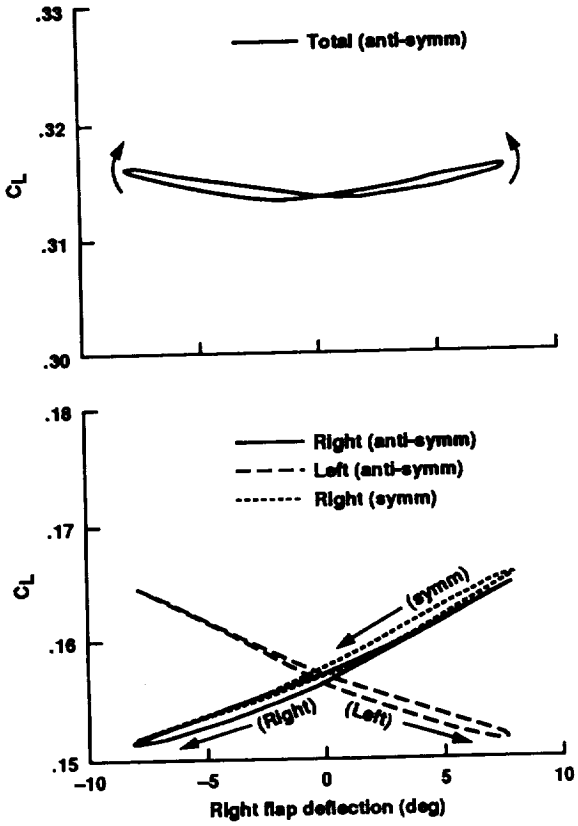


**Fig. 12 Comparison of lift responses between the symmetric and antisymmetric oscillatory motions of the flaps.**

of the primary vortex with the flap deflected down (the stronger side), but increases the strength with the flap up (the weaker side). As a result, the hysteresis appears during the flap deflected up in the antisymmetric case.

## Conclusions

Unsteady Navier–Stokes simulations of vortical flows in the transonic regime over a rigid arrow-wing configuration with trailing-edge control surfaces have been performed. Computations have been made at a moderate angle of attack, where a leading-edge separation occurs. Computed steady pressures and integrated force coefficients with and without control surface deflection show good agreement with the experimental data.

A comparison of response characteristics between the symmetric and antisymmetric control surface oscillatory motions on the left and right wings is also presented. For unsteady computations, the grid moves every time step following the deflection of the control surface. The antisymmetric case produces higher lift than the steady case with no deflection, and the symmetric case produces higher lift than the antisymmetric case. The unsteady pressure responses indicate strong influence of the flap motion at the flap trailing edge for both symmetric and antisymmetric cases. The detailed analysis of the wake structure revealed a strong interaction between the primary vortex and the wake vortex sheet from the flap region.

## References

[1]Manro, M. E., Manning, K. J. R., Hallstaff, T. H., and Rogers, J. T., "Transonic Pressure Measurements and Comparison of Theory to Experiment for an Arrow-Wing Configuration," NASA CR-2610, Aug. 1976.

[2]Ruhlin, C. L., and Pratt-Barlow, C. R., "Transonic Flutter Study of a Wind-Tunnel Model of an Arrow-Wing Supersonic Transport," AIAA Paper 81-0654, April 1981.

[3]Guruswamy, G. P., "Navier-Stokes Computations on Swept-Tapered Wings, Including Flexibility," AIAA Paper 90-1152, April 1990.

[4]Obayashi, S., Guruswamy, G. P., and Goorjian, P. M., "Streamwise Upwind Algorithm for Computing Unsteady Transonic Flows Past Oscillating Wings," *AIAA Journal*, Vol. 29, No. 10, 1991, pp. 1668–1677; also *AIAA Journal*, Vol. 30, No. 2, 1992, pp. 569 (Errata).

[5]Obayashi, S., and Guruswamy, G. P., "Unsteady Shock-Vortex Interaction on a Flexible Delta Wing," *Journal of Aircraft*, Vol. 29, No. 5, 1992, pp. 790–798.

[6]Obayashi, S., and Guruswamy, G. P., "Navier-Stokes Computations for Oscillating Control Surfaces," *Journal of Aircraft*, Vol. 31, No. 3, 1994, pp. 631–636.

[7]Baldwin, B. S., and Lomax, H., "Thin-Layer Approximation and Algebraic Model for Separated Turbulent Flows," AIAA Paper 78-257, Jan. 1978.

[8]Degani, D., and Schiff, L. B., "Computations of Turbulent Supersonic Flows Around Pointed Bodies Having Crossflow Separation," *Journal of Computational Physics*, Vol. 66, No. 1, 1986, pp. 173–196.

[9]"ICEM-CFD User's Guide Version 3.0," Control Data Technical Publications Aug. 1992.

[10]Chan, W. M., and Steger, J. L., "Enhancement of a Three Dimensional Hyperbolic Grid Generation Scheme," *Applied Mathematics and Computation*, Vol. 51, Oct. 1992, pp. 181–205.